JACS
JOURNAL OF THE AMERICAN CHEMICAL SOCIETY

Article

pubs.acs.org/JACS

Measuring and Predicting the Internal Structure of Semiconductor Nanocrystals through Raman Spectroscopy

Prabuddha Mukherjee,[†,‡] Sung Jun Lim,[†,§] Tomasz P. Wrobel,[‡] Rohit Bhargava,*[,†,‡,∥] and Andrew M. Smith*[,†,§,⊥]

[†]Department of Bioengineering, University of Illinois at Urbana−Champaign, Urbana, Illinois 61801, United States

[‡]Beckman Institute for Advanced Science and Technology, University of Illinois at Urbana−Champaign, Urbana, Illinois 61801, United States

[§]Micro and Nanotechnology Laboratory, University of Illinois at Urbana−Champaign, Urbana, Illinois 61801, United States

[∥]Departments of Chemical & Biomolecular Engineering, Electrical & Computer Engineering, Mechanical Science & Engineering and Chemistry, University of Illinois at Urbana−Champaign, Urbana, Illinois 61801, United States

[⊥]Department of Materials Science & Engineering, University of Illinois at Urbana−Champaign, Urbana, Illinois 61801, United States

Supporting Information

ABSTRACT: Nanocrystals composed of mixed chemical domains have diverse properties that are driving their integration in next-generation electronics, light sources, and biosensors. However, the precise spatial distribution of elements within these particles is difficult to measure and control, yet profoundly impacts their quality and performance. Here we synthesized a unique series of 42 different quantum dot nanocrystals, composed of two chemical domains (CdS:CdSe), arranged in 7 alloy and (core)shell structural classes. Chemometric analyses of far-field Raman spectra accurately classified their internal structures from their vibrational signatures. These classifications provide direct insight into the elemental arrangement of the alloy as well as an independent prediction of fluorescence quantum yield. This nondestructive, rapid approach can be broadly applied to greatly enhance our capacity to measure, predict and monitor multicomponent nanomaterials for precise tuning of their structures and properties.

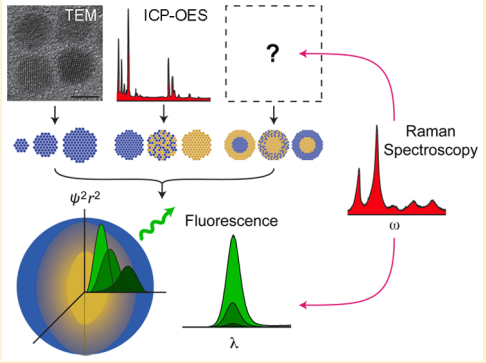

INTRODUCTION

Heterostructured nanocrystals (H-NCs) are a diverse class of materials with multiple chemical domains that provide novel and continuously tunable optical, electronic, chemical, and physical properties, as well as multifunctionality.[1−16] Semiconductor quantum dots (QDs) are a major class of H-NCs that are widely studied and applied due to unique advantages as light-emitting and light-harvesting materials for LEDs, solar cells, and biological imaging.[1,17−22] The properties and quality of QDs are profoundly impacted by the structural arrangement of their constituent chemicals. Abrupt (core)shell interfaces yield continuously tunable fluorescence wavelengths, emission efficiencies, brightness, excited state lifetimes, and charge localization.[1,17−22] When sharp (core)shell interfaces are smoothed into gradients, it is further possible to tune mechanical strain, defect density, and nonlinear optical effects such as the generation of multiple charge carriers from a single excitation photon.[11,23,24] For homogeneously mixed alloys, properties are uniformly tuned by Vegard's Law.[25] Therefore, knowledge of the internal structure is critical for the study, precise engineering, and application of H-NCs. Unfortunately, whereas H-NC size, morphology, and composition are readily determined using standard analytical measurements like transmission electron microscopy (TEM) and mass spectrometry, the internal structure cannot be distinguished with high accuracy. These crystals are usually just ∼10−20 atomic layers wide, so it is challenging to distinguish between alloys and (core)shell materials which may differ by just tens of atoms over several lattice planes. Single-particle techniques like TEM with elemental mapping are not sufficiently sensitive, and ensemble methods like X-ray crystallography do not provide chemical selectivity for H-NCs with dispersed sizes. Thus, there is a clear and urgent need for facile methods that allow detailed analysis of H-NC internal structure.

Here we report the accurate prediction of internal structure and optical properties of nanocrystal heterostructures using far-field Raman spectroscopy using a chemometric classification scheme. Raman spectroscopy is an information-rich technique that may be able to fill the void of internal structure determination by providing atomic vibrational modes indicative of local elemental environments, strain-induced deformations, and alloying. In H-NC internal structure assessment, the subtle difference between an alloy and a (core)shell material, for

Received: April 15, 2016
Published: July 29, 2016

DOI: 10.1021/jacs.6b03907
J. Am. Chem. Soc. 2016, 138, 10887−10896

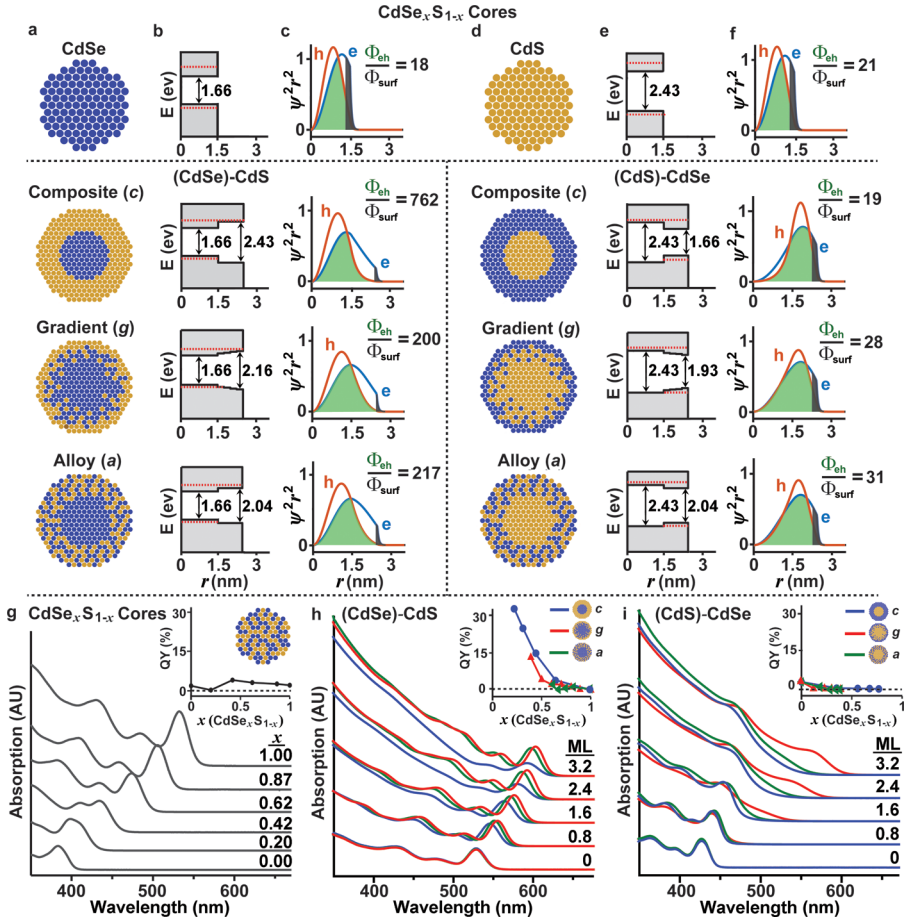

Figure 1. Heterostructured nanocrystal structure, electronic properties, and optical properties. (a,d) Schematics of H-NCs (b,e) electronic band structure, and (c,f) radial distribution functions of the electron (blue) and hole (red) in nm^{-1} units. Cores composed of CdSe are shown in (a−c) and cores composed of CdS are shown in (d−f). In (b) and (e), gray shaded areas show the bulk band structure and red dotted lines show the kinetic energy levels due to quantum confinement. In (c) and (f), the green shaded regions correspond to the overlap of the electron and hole wave function, Φ_{eh}, and the black shaded regions show the electron wave function overlap with the surface, Φ_{surf}. The ratio of their overlap, Φ_{eh}/Φ_{surf}, indicates the probability of the electron−hole recombination. (g) Absorption spectra of a series of alloy CdSe$_x$S$_{1-x}$ cores for a range of x values between 0 and 1. The inset shows the dependence of the measured *QY* on composition x. (h) Absorption spectra of (core)shell QDs with CdSe cores and three different internal structures as a function of shell monolayers (ML). The inset shows the dependence of the measured *QY* on composition x of the entire nanocrystal. (i) Absorption spectra of (core)shell QDs with CdS cores and three different internal structures as a function of shell monolayers (ML). The inset shows the dependence of the measured *QY* on composition x of the entire nanocrystal. AU = arbitrary units.

example, should manifest itself in a redistribution of bond strain and electronic polarization between different atoms. Raman spectroscopy has already been applied for interpreting H-NCs;[26−28] however, it has not been possible to integrate data into a complete understanding of nanocrystal structure due to the lack of comparisons with theoretical atomistic models,[29,30] which are neither sufficiently accurate nor high throughput for simulating H-NCs with realistic sizes (>3 nm, >500 atoms). Here we show that spectral measurements allow the generation of predictive models of internal structure. Furthermore, it is well-known that subtle structural differences in H-NCs can dramatically alter their quantum yield (*QY*), which is difficult to predict. Hence, we extended our approach to predict *QY* with this nondestructive, far-field method using widely available instrumentation.

RESULTS AND DISCUSSION

Heterostructured Nanocrystal Designs. Figure 1a−f shows the design of 7 classes of CdS:CdSe QDs. The first class is a series of homogeneous QDs comprising binary CdS and CdSe nanocrystals with controlled sizes (2−6 nm diameter), and CdSe$_x$S$_{1-x}$ alloys spanning the full range of ternary compositions (x = 0 to 1). We further synthesized 6 classes of (core)shell QDs with precisely controlled domains that span the full range of abrupt interfacial *composites* (*c*), smooth *gradients* (*g*), and homogeneous *alloys* (*a*), with both CdS and CdSe cores and both CdS and CdSe shells. We designate these 6 materials as (core)-*c*-(shell), (core)-*a*-(shell), and (core)-*g*-(shell), respectively. In the case of *alloys*, the shell composition is actually CdS$_{0.5}$Se$_{0.5}$ but denoted by CdS or CdSe for brevity. Each (core)shell structure was made in a series of 4 or 5 variants, one of each of which uniquely provided the same total CdS$_x$Se$_{1-x}$ composition across all of the classes. With this synthesis scheme, we were able to prepare diverse internal structures with either identical QD sizes or identical QD compositions for direct comparisons. A total of 42 QD structures were prepared with the same synthetic conditions, as detailed in the Experimental Section. The (core)shell QDs were synthesized using successive ion layer atomic adsorption and reaction (SILAR) processes so that sequential monolayers

DOI: 10.1021/jacs.6b03907
J. Am. Chem. Soc. 2016, 138, 10887−10896

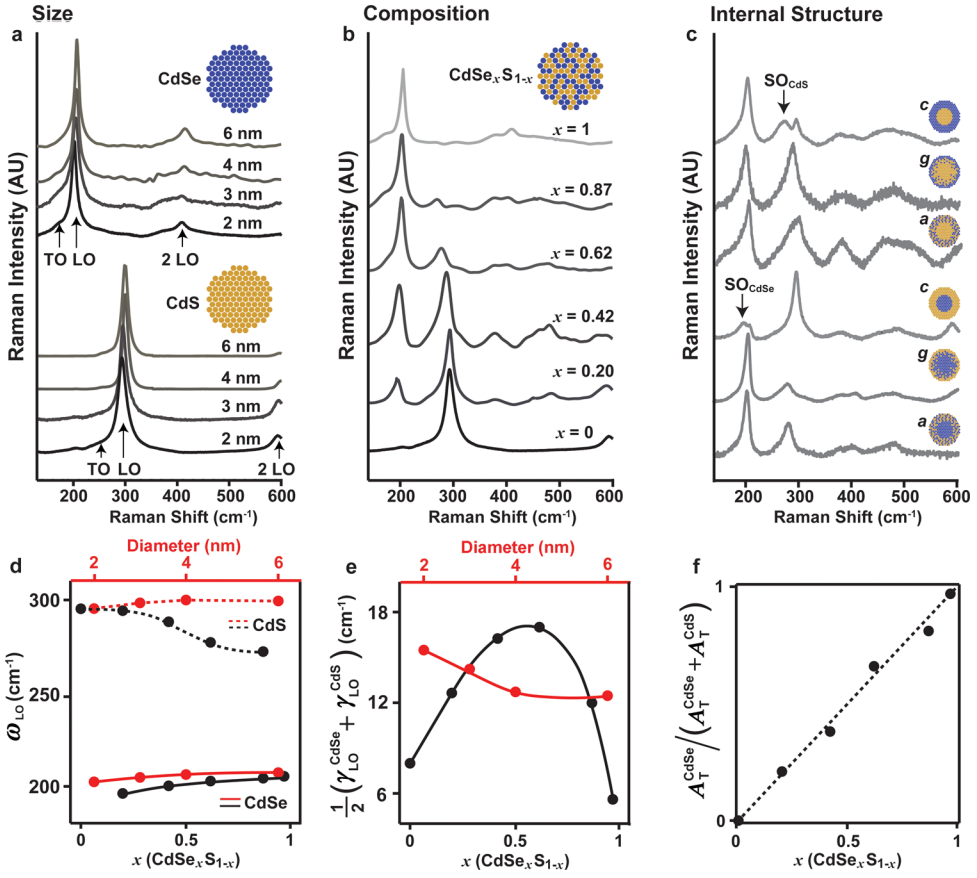

Figure 2. Raman spectroscopic characterization of CdS:CdSe H-NCs. (a) Raman spectra of different sizes of binary CdSe (top) and CdS (bottom) nanocrystals. (b) Raman spectra of different compositions, x, of $CdSe_xS_{1-x}$ ternary alloy cores. (c) Raman spectra of (core)shell H-NCs with either CdS cores (top three) or CdSe cores (bottom three) with either composite, gradient, or alloy internal structures. AU = arbitrary units. (d) Frequencies of CdS and CdSe LO modes for different size binary cores (red; top x-axis) and different ternary alloy core compositions (black; bottom x-axis). (e) Average total line widths of CdSe and CdS LO modes for different size binary cores (red; top x-axis) and different ternary alloy core compositions (black; bottom x-axis). Widths were extracted by fitting spectra to sums of Lorentzian functions. (f) Ratio of the total area of the fundamental CdSe modes with respect to the total area of the CdSe and CdS fundamental modes as a function of ternary alloy core composition.

were deposited with precisely controlled composition by adjusting the S:Se stoichiometry with each precursor addition. Previous results have shown that the low deposition temperature (190 °C) prevents diffusive alloying between S and Se atoms.[31−33] TEM verified spherical morphologies of the QDs (Supporting Figure S1), and composition was verified by elemental analysis (see Experimental Section). Because the ligands and purification processes were the same for all samples, all materials and optical properties are expected to solely depend on the internal structure, rather than the surface, which often dominates optical effects.

Optical and Electronic Properties. Figure 1b and 1e depict energy band diagrams of the electron (e) and hole (h) for each nanocrystal along the radial dimension (r), showing both bulk energy bands (gray) and quantum-confined kinetic energy levels (red) calculated using the effective mass approximation assuming spherical symmetry and finite energy wells.[34] Figure 1c and 1f depict radial distribution functions (RDF, ψ^2r^2) of the electronic wave functions (ψ_e and ψ_h), which we used to calculate overlap integrals between the electron and hole (Φ_{eh}) as well as surface overlap integral (Φ_{surf}). These two parameters are believed to largely dictate fluorescence QY as the probability of electron−hole recombination diminished by surface trap states.[35−37] We show their ratio, Φ_{eh}/Φ_{surf}, for which larger values should generally correlate with higher QY. Importantly, the (core)shell nanocrystals fell within two distinct QY classes depending on whether charge carriers were primarily localized in the core (CdSe cores) or in the shell (CdS cores), which has a major impact on electronic and optical properties. CdSe-core QDs have a high Φ_{eh}/Φ_{surf} (~200−800), providing a high QY that is useful for applications in emitting devices and sensors. CdS-core QDs have low Φ_{eh}/Φ_{surf} (~20−30), leading to low QY that enables applications in photovoltaic devices requiring efficient charge extraction.

Optical absorption spectra of these materials are shown in Figure 1g−i. Spectra of homogeneous $CdSe_xS_{1-x}$ alloy cores shift proportionally to x (Figure 1g), in accord with Vegard's Law with bowing.[38] The internal structural differences had subtle impacts on optical absorption features of (core)shell nanocrystals with CdSe cores (Figure 1h) and CdS cores (Figure 1i). For all materials, growth of a shell material reduced the bandgap, consistent with relaxation of quantum confinement by allowing charge carriers to expand. For (core)shell QDs with CdSe cores, the internal structure had a major impact on QY (Figure 1h inset), following the trend $c > g \sim a$, which is consistent with Φ_{eh}/Φ_{surf} predictions. QY for the core-only QDs and (core)shell QDs with CdS cores was low and close to zero (Figure 1g, 1i insets).

DOI: 10.1021/jacs.6b03907
J. Am. Chem. Soc. 2016, 138, 10887−10896

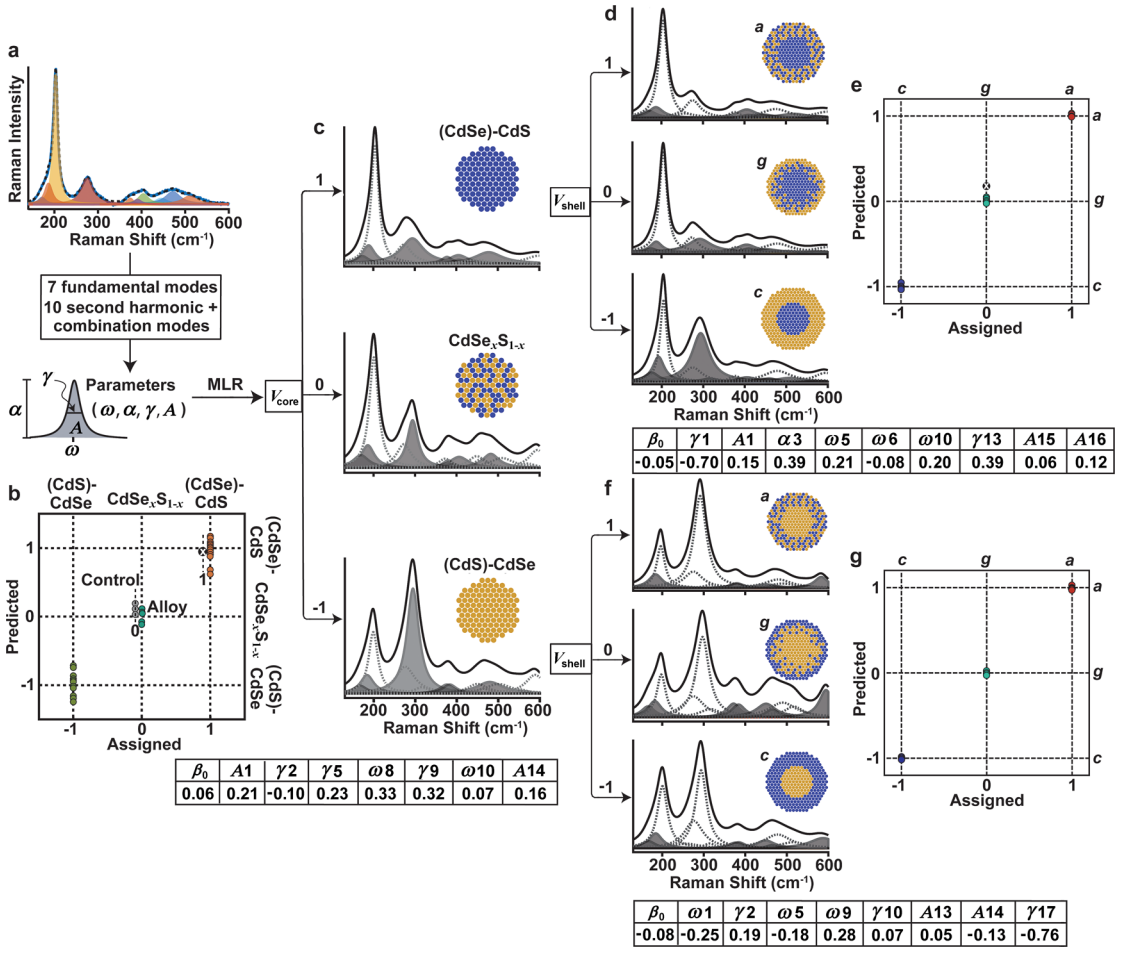

β_0	$\gamma 1$	$A1$	$\alpha 3$	$\omega 5$	$\omega 6$	$\omega 10$	$\gamma 13$	$A15$	$A16$
-0.05	-0.70	0.15	0.39	0.21	-0.08	0.20	0.39	0.06	0.12

β_0	$A1$	$\gamma 2$	$\gamma 5$	$\omega 8$	$\gamma 9$	$\omega 10$	$A14$
0.06	0.21	-0.10	0.23	0.33	0.32	0.07	0.16

β_0	$\omega 1$	$\gamma 2$	$\omega 5$	$\omega 9$	$\gamma 10$	$A13$	$A14$	$\gamma 17$
-0.08	-0.25	0.19	-0.18	0.28	0.07	0.05	-0.13	-0.76

Figure 3. Chemometric analysis of CdS:CdSe H-NC internal structure. (a) Measured spectra are fit to a sum of Lorentzian functions to yield 4 parameters per function, and spectra are assigned to a core class variable V_{core}. (b) MLR allows the prediction of structure based on the assigned class variable, showing accurate classification of all H-NCs. Three alloys (gray) and one (CdSe)CdS QD (black with x) were used afterward to validate the classification. (c) Simulated Raman spectra from the extracted MLR parameters show the average spectrum for each core class (black curve) as well as the most important parameters for class distinction (shaded curves). The parameters are tabulated below the spectra. (d, e) Different shell classes are assigned to a variable V_{shell} for MLR classification. Simulated Raman spectra show the average spectrum, the most important contributors, and tabulated parameters as in part (c). (f, g) Successful MLR prediction of internal structures of (CdS)-CdSe and (CdSe)-CdS as composites, gradients and alloys.

Raman Spectral Signatures. Raman spectra of these QDs are shown in Figure 2, demonstrating the effect of tuning size (Figure 2a), composition of $CdSe_xS_{1-x}$ alloy cores (Figure 2b), and internal structure of (CdSe)-CdS and (CdS)-CdSe composites, gradients, and alloys (Figure 2c). These II–VI materials were synthesized with zinc blende crystal lattices in which each atom is tetrahedrally coordinated with 4 nearest neighbors. With this bonding symmetry, 2 distinguishable Raman peaks are observed as the longitudinal optical (LO) and transverse optical (TO) modes, shown for CdS and CdSe core QDs in Figure 2a with their first harmonic peaks (2 × LO).[29,39,40] LO peaks dominate the spectra and the TO peaks on the low frequency sides are almost undetectable, as they are buried in surface-related modes (see below).[27,41] The significant frequency (or wavenumber) difference between LO_{CdS} and LO_{CdSe} derives from differences in bond vibrational frequencies in each nanocrystal, as Cd–S bonds are shorter and stronger (i.e., larger spring constant) than Cd–Se bonds. This provides a useful independent probe of Cd–S and Cd–Se bonds, and the fundamental vibrational frequency is relatively independent of nanocrystal size, as summarized in Figure 2d. In our analysis below, we only use the 140–600 cm^{-1} range plotted in Figure 2; example spectra over a wider range are shown in Supporting Figure S2.

Figure 2b shows that when CdS and CdSe are homogeneously mixed in $CdSe_xS_{1-x}$ alloy cores, independent contributions of Cd–S and Cd–Se bonds remain spectrally distinct. This is a unique feature of Raman spectroscopy compared to other scattering techniques like X-ray diffraction for which long-range crystal coherence effects dominate to average across bond lengths, reflecting Vegard's Law. With Raman spectroscopy, contributions from the different chemicals are clearly resolved, which is consistent with bulk measurements of $CdSe_xS_{1-x}$ alloys as two-mode phonon materials.[49] This provides a probe of short-range local chemical environments. Two distinct features arise when CdS and CdSe are blended as $CdSe_xS_{1-x}$ alloys; first the LO frequencies shift, especially for the CdS peak, which moves to lower frequency as x increases (Figure 2d), indicating a weaker, longer bond. In fact, previous studies have shown that the frequency difference between the LO_{CdSe} and LO_{CdS} peaks strongly correlates with composition (see Supporting Figure S3).[41,43] Second, all peaks broaden as the composition approaches x = 0.5 (Figure 2e), reflecting heterogeneous Cd–Se and Cd–S bond environ-

DOI: 10.1021/jacs.6b03907
J. Am. Chem. Soc. 2016, 138, 10887–10896

ments.[41] Therefore, for a fixed size, the CdS frequency and bandwidth are excellent probes for measuring alloying. Note that the bandwidth shifts with size, but to a much smaller degree than for alloying (Figure 2e). Figure 2f summarizes another important feature of alloys: the integrated areas of LO_{CdS} and LO_{CdSe} are nearly proportional to their chemical concentrations in the nanocrystal. This is expected because transition strengths are dictated by electronic dipole coupling, and the ionicities (f) of CdS and CdSe are similar (f_{CdS} = 0.59 and f_{CdSe} = 0.58 by Pauling values) and their bonding geometries are identical. Electronic resonance can play a role as well, as discussed below.

Figure 2c shows Raman spectra representative of the six classes of (core)shell QDs. Spectra smoothly transition from those of the core to the (core)shell during shell growth (Supporting Figure S4). The spectra are clearly more complex than those of the simple binary and ternary cores, deriving from a convolution of multiple chemical as well as structural domains. Notably while their optical absorption spectra (Figure 1g–i) were only subtly different between classes with CdSe cores or with CdS cores, their Raman spectra have distinctive features for each class, reflecting distinct local chemical domains. For example, composite materials have a new peak at the low-frequency shoulder of the core LO peak. This peak was previously assigned as a surface optical (SO) mode,[44] indicating the presence of a distinctly resonant structural interface. There is also rich information in harmonic regions of the spectrum, which were previously analyzed to assign peaks for some CdS:CdSe H-NC composites.[27,39] These higher harmonic vibrations can exhibit new combination bands derived from coupled vibrations between nearby bonds and therefore reflect longer-range structure compared with the first order region of fundamental bond vibrations.[45] Clearly, signatures from these chemical domains are present with distinctive vibrational energies, strengths, and bandwidths, but their convolution prevents direct intuitive use for internal structure determination.

Chemometric Models for Structure Classification and Prediction. As shown in Figure 3, we developed a chemometric approach to internal structure classification. We analyzed Raman spectra of each of the 7 QD classes by multivariate methods: principal component analysis (PCA)[46] and multiple linear regression (MLR).[47] PCA is a model-free approach for determination of contributors to variance while MLR can reduce the complexity of multivariate analysis by identification of the importance of variables in a linear regression. First we deconstructed each spectrum of convolved, asymmetric Raman peaks into a sum of Lorentzian functions. To do so, we used PCA to determine the number of modes contributing to each data set and found that the fundamental CdSe region (140–242 cm^{-1}) arose from at least 4 sources of variance and the fundamental CdS region (242–350 cm^{-1}) derived from at least 3 sources, based on Malinowski's criteria.[46] Hence, we chose 7 Lorentzian functions for the spectral region originating from fundamental modes, likely arising from TO, SO and LO modes, plus an additional mode between the LO_{CdSe} and LO_{CdS} peaks that may derive from surface effects or acoustic phonons.[27,48] This latter mode did not factor significantly into the classification model. Ten additional functions were used to fit the second harmonic range (350–600 cm^{-1}). Thus, each spectrum $S(\omega)$ was fit to 17 Lorentzian curves (Figure 3a):

$$S(\omega) = \sum_{i=1}^{17} \alpha_i \frac{\gamma_i}{(\omega - \omega_i)^2 + \gamma_i^2} \quad (1)$$

where the parameters ω_i, γ_i, and α_i are the frequency, full-width at half-maximum (fwhm), and amplitude of the i-th spectral peak. A fourth parameter A_i is the area under the i-th curve which is redundant with the combination of γ_i and α_i, but included as a useful classification metric. All parameters are provided in Supporting Table S1.

We then assigned Raman spectra to different structural classes using a two-step fitting process. First a class variable, V_{core}, assigns the known core type and then a subclass variable, V_{shell}, assigns a shell type. In the first step (Figure 3b and 3c), Raman spectroscopy of QDs with cores of CdSe (V_{core} = 1), $CdSe_xS_{1-x}$ (V_{core} = 0), or CdS (V_{core} = −1) were classified using MLR:

$$V = \beta_0 + \sum_i \sum_{j=\omega,\gamma,\alpha,A} C_{ij}(k_{ij} - \overline{k_{ij}}) \quad (2)$$

where k_{ij} values are the ω_i, γ_i, α_i and A_i parameters from Lorentzian functions corresponding to the j-th value and i-th peak, $\overline{k_{ij}}$ is their mean used for centering, and C_{ij} values are the output parameters quantifying the magnitude of importance to class type distinctions. β_0 is an offset and the k_{ij} parameters were normalized to unity variance so each was weighted equally. The predicted values for the internal structures based on the core materials are plotted against the assigned V_{core} values in Figure 3b. All 36 QDs were correctly classified; the relative spread of the predicted values partially reflects the range of the continuous composition variable x. The fitted C_{ij} values indicate the origin of differences between each of the classes and the values are shown in Figure 3c with theoretical spectra. Solid black curves represent the average predicted value overlaid on contributing Lorentzian peaks, with peaks shaded to indicate those most heavily weighted in the classification. In the second step, we assigned V_{shell} to distinguish the internal structures of (core)shell materials, predicting three subclasses as alloys (V_{shell} = 1), gradients (V_{shell} = 0), and composites (V_{shell} = −1). The fitted C_{ij} values are also summarized with theoretical spectra in Figure 3d and 3f. Again, all 28 QDs were correctly classified (Figure 3e and 3g).

It is important to note that it is impossible to be fully comprehensive of all possible combinations of size, composition, and internal structure. However, we have determined that size has a relatively small impact on spectral features compared with composition (Figure 2d and 2e) and our designed structures include a comprehensive set of architectures and compositions (Supporting Table S2 and S3). Hence, we expect that this classification scheme can be applied to any CdS:CdSe material. We externally validated this hypothesis by testing 3 additional Raman spectra not included in the initial classification (Supporting Figure S4 and S5): two alloy cores generated using literature methods (gray circles in Figure 3b) and one (CdSe)-g-CdS QD (black-cross circle in Figure 3e). All three were accurately classified, and we additionally tested one unknown sample that we synthesized using a new method, which was classified also as an alloy core (Supporting Figure S3).

In addition to accurately determining internal structure, this classification scheme also provides mechanistic structure–function relationships between Raman spectra and internal structure. The clearest trends were evident in fundamental

DOI: 10.1021/jacs.6b03907
J. Am. Chem. Soc. 2016, 138, 10887–10896

modes. In core-class distinction, two parameters were most heavily weighted—the area of the CdSe shoulder (indicating the SO_{CdSe} mode) and the width of the LO_{CdS} peak (indicating the degree of alloying). In accord with the lack of shift of LO_{CdSe} with size or composition (Figure 2d and 2e), this peak was never a strong consideration in any of the classifications. That is, its intensity and width were not a consistently distinguishing spectral feature. For the (core)shell materials with CdSe cores, the defining features were the SO_{CdSe} peak, its second harmonic, and the LO_{CdS} peak. For the (core)shell materials with CdS cores, the fundamental CdS peak did not provide any distinguishing contribution, but its second harmonic peak was heavily weighted likely due to its indication of longer distance interactions. We found that fundamental modes alone were never sufficient for analysis and always had to include the harmonic features, which are very challenging to distinguish and manually interpret,[27] but for which multivariate analysis is ideally suited for predictive modeling.

Quantum Yield Classification. We next used a similar classification algorithm to determine if we could accurately predict *QY*, without knowledge of the internal structure. We found that a linear algebraic model needed only two parameters C_{ij} from the fundamental mode spectral region for accurate prediction:

$$QY = \beta_0 + C_{\alpha_5}(\alpha_5 - \overline{\alpha_5}) + C_{\gamma_1}(\gamma_1 - \overline{\gamma_1}) \quad (3)$$

As shown in Figure 4a, the predicted *QY* was in good agreement (R^2 = 0.98) with the measured *QY* values for

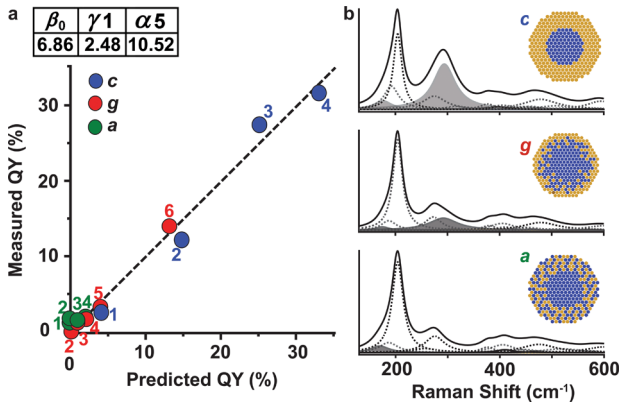

Figure 4. Chemometric prediction of H-NC optical properties. (a) Prediction of the quantum yield of QDs with CdSe cores. MLR parameters are tabulated above the plot. Numbers in for each point correspond to shell thickness numbers in Supporting Table S1. (b) Simulated Raman spectra corresponding to a composite, gradient, and alloy nanocrystal that exhibit high to low *QY*.

(core)shell materials with CdSe cores. We did not include QDs with CdS cores because *QY* values were expectedly low and also could not be accurately measured. Figure 4b shows the average spectra of (CdSe)CdS QDs with different internal structures as well as the model parameters. The shaded peaks distinguish the influence of two critical parameters on the *QY* prediction: the amount of shell material (intensity of LO_{CdS}, α_5) as well as the abruptness of the shell interface (width of SO_{CdSe} γ_1), which is consistent with the theoretical EMA model (Figure 1c). The composite QD exhibits an intense LO_{CdS} mode originating from the unalloyed shell as well as a broad SO_{CdSe} peak that contributes to the high *QY*. For the gradient and alloy QDs, the CdS peaks are substantially weaker and shifted to lower wavenumbers due to alloying, and the SO_{CdSe} peak is weaker due to the lack of a distinct interface. Importantly, this *QY* is derived from Raman spectra without any additional information other than the chemical composition of the core. To our knowledge, this is the first time that spectral classification has allowed the accurate prediction of H-NC structures as well as key emergent properties such as quantum yield.

Extension to Other H-NC Materials. It is important to evaluate the extent to which we can expect these parametric classifications to extrapolate to other H-NC materials. As stated above, size has only a small impact on the Raman spectra, and we evaluated a wide range of CdS:CdSe compositions and internal structures, so we expect that these classifications will be valid for nearly any CdS:CdSe H-NC. Furthermore, we also expect for these classifications to be valid if we switch elemental composition, but both the peak fitting process and the specific k_{ij} parameters may need to be recalibrated to account for the altered phonon modes. We break down the expected perturbations, and how to account for them, based on six effects: phonon mode class, strain, defects, electronic dipole effects, ligands, and sample heterogeneity.

Phonon Mode Class. In general, we expect that these trends will hold for most ternary H-NCs with zinc blende or wurtzite crystal structures with II−VI and III−V compositions. In particular, all ternary II−VI materials with a common metal, such as CdSe:CdTe and ZnSe:ZnS, are two-phonon mode across all composition ranges, which is also the case for most III−V materials.[42] This is also the case for many, but not all, ternary materials with common anions (S, Se, or Te), including ZnTe:CdTe and CdTe:HgTe. The Raman spectra of these H-NCs are expected to follow the classification trends of our k_{ij} parameters (scaled as described below), but the peak frequencies must to be shifted to those of the constituent binary materials. The most effective way to do this would be by calibrating the peak fitting process using QDs of the new binary material(s). However, some ternary materials do not exhibit two distinguishable phonon modes over all composition ranges due to the close frequencies of their constituent LO modes.[42] Such single-mode or intermediate-mode materials notably include common-anion CdS:ZnS and CdSe:ZnSe, which would be challenging to classify by our metrics alone due to the challenge of precise peak fitting to yield accurate k_{ij} parameters; these H-NCs would likely require a diverse set of calibration standards, following our methodologies. Importantly, these classifications are not expected to translate to quaternary materials such as CdSe:ZnS, for which three or four distinct phonon modes will be present due to the additional presence of Cd−Se and Zn−Se bonds, yielding more complex spectra. We are working to classify these spectra as well.

Strain. In order to apply these classifications to different materials that exhibit compatible alloy phonon modes, it will be necessary to scale the parameters appropriately to account for strain.[27,50,51] For an example case of switching CdS:CdSe to CdS:CdTe, because CdTe has a larger bond length than CdSe (a_{CdSe} = 6.05 Å; a_{CdTe} = 6.48 Å), its greater bond length mismatch with CdS (a_{CdS} = 5.82 Å) will cause a greater distortion of Cd−S bonds (tensile strain), and the new Cd−Te bonds will exhibit greater compression than Cd−Se bonds.[11] This effect will increase both the frequency shifts and bandwidths of the phonon modes. To account for this, the k_{ij} parameters ω_i and γ_i should be scaled by the bond length differential (165% increase), α_i should be scaled inversely, and the modes specifically derived from CdTe should be scaled to

DOI: 10.1021/jacs.6b03907
J. Am. Chem. Soc. 2016, 138, 10887−10896

account for the new phonon deformation potential compared with CdSe.

Defects. General trends observed for our classifications will only remain valid for other materials systems as long as the lattice is coherent (defect-free). CdS:CdSe H-NCs should remain defect-free and monocrystalline throughout growth for all of the H-NC classes, but composite structures composed of materials with highly mismatched bond lengths will induce the formation of defects (e.g., dislocation loops) to relax strain beyond a specific critical thickness of shell.[11,37] This will yield large deviations from our observed trends, but these deviations can also be a sensitive means to detect and characterize specific defects that have so far eluded conventional H-NC characterization methods like electron microscopy. However, certain types of defects like cubic-hexagonal stacking faults are not expected to yield major differences in the first order spectral ranges due to the retention of tetrahedral bonding in all crystal phases of the H-NCs,[52] however some deviations may be present in the higher order spectral ranges where effects from longer range interactions can be amplified for a switch between T_d and C_{3v} symmetries. Polycrystallinity resulting from non-tetrahedral coordination (e.g., IV−VI materials like PbSe) would be expected to drastically alter the results.

Electronic Dipole Effects. Materials with different electronic polarization and electronic resonances are also expected to result in a deviation from our observed trends by changing the intensities of specific peaks. Different material ionicities will yield different nonresonant vibrational mode intensities, which will alter peak intensities. This is only expected to have a minor impact for II−VI materials, which have only a small range of ionicities (f = 0.52−0.59), but this can be more substantial for III−V materials (f = 0.25−0.56).[49] To account for this, k_{ij} parameters α_i and A_i should be scaled proportionally. Also if an excitation source is chosen such that significant electronic excitation occurs (resonance Raman), this can substantially enhance the intensities of phonon modes coupled to the transition.[53] Some of the H-NCs evaluated in this work were in the resonance range of our 532 nm beam which can excite some of the CdSe peak modes (see Figure 1g−i). While this is expected to have an effect on peak intensities, the effect on our classification parameters is expected to be very small, as LO_{CdSe} was not an important factor in the classifications (see Figure 3). If materials are used that could be substantially impacted by electronic resonance, our classifications will likely be in stronger accord by using laser energies that avoid electronic transitions.

Ligands. It is also important to note that surface ligands can impact Raman spectra of nanocrystals. Small peak shifts and intensity changes have been observed for QDs when their ligands are exchanged or when synthesized with different ligands in solution.[50,54] In our case, prior to evaluation of these H-NC sets, we evaluated the impact of ligands on the Raman spectra, and observed that some sets (carboxylates and phosphonates used here) did not substantially impact the spectra, but others (thiols) did have a marked effect (see Supporting Figure S6). Ligands are expected to selectively modulate surface atoms, which are an important part of the materials under study, which justifies our use of our experimental setup in which the ligands were fixed for all of the materials. This is also critical for evaluation of a parameter like *QY*, which is dominated by surface effects for most QDs.[55] Importantly, extrapolation of these findings to other materials for *QY* will likely only be effective when the materials exhibit similar band offsets, and when ligands and solvents are strictly controlled so that impacts of internal structure alone are manifested.

Sample Heterogeneity. Raman spectroscopy is a far-field technique that yields population-averaged signals from samples that can be heterogeneous in both structure and composition. In our case, we made great efforts to maximize homogeneity by using nearly monodisperse cores and highly controlled shell deposition methods to precisely control composition, layer-by-layer. In fact, the relative standard deviation in size improved from the cores (∼10%) to the (core)shell materials (4−8%) (Supporting Figure S1), and the highly discrete nature of the electronic transitions was indicative of compositional homogeneity (Figure 1). If we were to use materials with greater polydispersity, we expect that the accuracy of our classification metrics to decrease.[43] However, size heterogeneity is not likely to play a major role, as size was not found to be a major factor in the Raman modes (Figure 2b, 2e). Instead, we expect that heterogeneity in composition would have the most significant impact. This is because $CdSe_xS_{1-x}$ is a nonstructured alloy that is expected to be compositionally random, that is, the composition distribution of individual QDs should fit to a beta distribution between x = 0−1 within an ensemble. A wide dispersion in composition would be expected to wash out distinguishing features of each class, as microdomains of each structure class would be present within each sample. Notably, if compositional dispersion is expected, it could be considered as part of our model, but we do not have an accurate measurement technique. Doing so in a direct manner with composition-sensitive electron microscopy is very challenging and low-throughput, and inferences from electronic transition bandwidths are convolved with size dispersion. It is also possible that microdomains of differing strain could have a similar outcome as compositional heterogeneity. For example, if shell growth is not spherically isotropic, as is frequently observed in the case of wurtzite materials, strain in the core will be different in the regions which have thicker or thinner shells. Thus, even for a perfectly abrupt composite structure without alloying, the impact would be more complex Raman features, such as a widening of the SO band and additional second harmonic features. If this also occurs in the presence of alloying, the mixtures of differing combinations of strain and composition could lead to the difficult condition of two different microdomains having equivalent vibrational modes, which would further reduce the classification accuracies. However, because homogeneity is such a critical need for almost most applications, we expect that the use of our approach on highly dispersed materials will not be common.

■ CONCLUSIONS

Here we classified internal structures and predicted emergent properties (quantum yield) of H-NCs using Raman spectroscopic measurements combined with chemometric analyses. While Raman spectroscopy has been used to characterize structure, strain, and defects of semiconductors, its application has largely been qualitatively due to the complexity of heterostructure spectra and the lack of accurate theoretical models for comparison. Our approach overcomes these limitations through precise materials synthesis, as well as modeling and prediction of structure−function relationships with multivariate analysis, which together yield critical insights into structures responsible for emergent properties. Current single-molecule and ensemble characterization methods do not provide this type of empirical prediction and insight. We expect

DOI: 10.1021/jacs.6b03907
J. Am. Chem. Soc. 2016, 138, 10887−10896

that this methodology will permit nondestructive monitoring of structure and quality during H-NC synthesis to allow unambiguous structural verification without extensive needs for computational modeling. This approach should be broadly applicable across different compositions with the imposition of correction terms based on lattice mismatch, crystal phase, and iconicity.

EXPERIMENTAL SECTION

Chemicals. Cadmium oxide (CdO, 99.99+%), selenium dioxide (SeO_2, ≥ 99.9%), selenium powder (Se, ∼100 mesh, 99.99%), sulfur powder (S, 99.98%), hexamethyldisilathiane ($(TMS)_2S$, synthesis grade), tributylphosphine (TBP, 97%), 1,2-hexadecanediol (HDD, 97%), tetramethylammonium hydroxide solution (TMAH, 25 wt % in methanol), tetradecane (TD, olefin free, ≥99.0%) and fluorescein isothiocyanate isomer I (fluorescein, ≥90%) were purchased from Sigma-Aldrich. Anhydrous cadmium chloride ($CdCl_2$, 99.99%) was from Alfa Aesar. 1-octadecene (ODE, 90% tech.), oleylamine (OLA, 80−90% C18-content), oleic acid (OAc, 90% tech.), and myristic acid (MAc, 99%) were purchased from Acros Organics. Behenic acid (BAc, 99%) was obtained from MP Biomedicals. Solvents including chloroform, hexane, methanol, and acetone were purchased from various suppliers including Acros Organics, Fisher Scientific, and Macron Fine Chemicals. All chemicals were used as purchased. Cadmium behenate ($Cd(BAc)_2$) was synthesized using methods described in the literature.[3] Tributylphosphine sulfide (TBPS, 1 M) and tributylphosphine selenide (TBPSe, 3.75 M) were prepared by mixing either S powder (1 mmol) and TBP (1 mL) or Se powder (3 mmol) and TBP (0.8 mL) in a 4 mL vial under nitrogen. Then the mixtures were sonicated at room temperature until becoming clear and colorless. S/ODE (0.1 M) and Se/ODE (0.1 M) stock solutions were prepared by dissolving S powder (1 mmol) or Se powder (1 mmol) in ODE (10 mL) at ∼200 °C under nitrogen.

H-NC Synthesis. *CdSe Cores.* CdSe cores were synthesized using methods reported previously.[3] Briefly, $Cd(BAc)_2$ (0.2 mmol), SeO_2 (0.2 mmol), HDD (0.2 mmol), and ODE (4 mL) were added to a 50 mL round-bottom flask (r.b.f.) and degassed under vacuum at ∼100 °C for 2 h. Then the temperature was ramped to 230 °C at a rate of ∼20 °C/min under nitrogen. After reaching 230 °C, the temperature was maintained for 15 min to induce nanoparticle growth. The reaction was quenched by reducing the temperature. When the temperature was reduced to ∼100 °C, the reaction mixture was diluted in chloroform (10 mL) containing OAc (1 mL) and OLA (0.6 mL). CdSe QDs were precipitated by adding a mixture of methanol (15 mL) and acetone (15 mL) and centrifuging at 7000*g* for 5 min. QDs were redispersed in hexane (∼20 mL) and extracted twice with methanol (10−15 mL per cycle) followed by precipitation with excess methanol to remove excess ligands and byproducts. Finally, pure QD precipitates were washed with acetone to remove residual methanol and dispersed in hexane as a stock solution.

CdS Cores. $Cd(BAc)_2$ (0.2 mmol) and ODE (4 mL) were added to a 50 mL r.b.f. and briefly (∼10 min) degassed under vacuum at ∼100 °C. The temperature was ramped to 230 °C at a rate of ∼20 °C/min. At 220 °C, TBPS (166 μL) was quickly injected to initiate CdS QD nucleation. After reaching 230 °C, the temperature was maintained for 60 min to induce further particle growth. As-synthesized CdS QDs were purified using the same procedure used for CdSe QDs.

$CdSe_xS_{1-x}$ Core. $CdSe_xS_{1-x}$ cores were synthesized using four different protocols from the literature.

1. Homogeneous $CdSe_xS_{1-x}$ Alloys.[3] A series of homogeneously alloyed $CdSe_xS_{1-x}$ cores (diameter = 2−3 nm) were synthesized and purified using the same protocol used for CdSe core synthesis except with a controlled ratio of SeO_2 and elemental S instead of SeO_2 alone. That is, a mixture of SeO_2 ($0.2 \times x$ mmol) and S ($0.2 \times (1 - x)$ mmol) with x varied as 0, 0.17, 0.33, 0.5, 0.67, and 1 was reacted with $Cd(BAc)_2$ (0.2 mmol) and HDD (0.2 mmol) in ODE (4 mL) at 230 °C for 15 min. Exact compositions of each homogeneous alloy cores were measured by elemental analysis.

2. Rosenthal Method 1 (Ros).[38] Homogeneously alloyed $CdSe_{0.5}S_{0.5}$ cores were synthesized using methods introduced by Rosenthal and co-workers. Briefly, CdO (1 mmol), OAc (4 mmol), and ODE (5 mL) were added to a 50 mL r.b.f. then heated at 310 °C until the mixture became a clear, colorless solution. A chalcogen precursor solution prepared by mixing TBPSe 3.75 M (0.25 mL), S/ODE 0.1 M (2.5 mL), and ODE (2.3 mL) was quickly injected at 315 °C to induce nucleation and QDs were grown at 270 °C for 4 min. The reaction was quenched by reducing the temperature. QDs were purified by precipitation with methanol and acetone multiple times. Finally, purified QDs were dispersed in hexane.

3. Hens Method (Hens).[56] Homogeneously alloyed $CdSe_{0.5}S_{0.5}$ cores were synthesized using methods reported by Hens and co-workers. CdO (0.2 mmol), MAc (0.6 mmol), and ODE (10 mL) were added to a 50 mL r.b.f. and heated to 270 °C until the mixture became a clear, colorless solution. The chalcogen precursor prepared by mixing S/ODE 0.1 M (0.5 mL) and Se/ODE 0.1 M (0.5 mL) was quickly injected at 260 °C to induce nucleation, and QDs were further grown for 5 min. Finally, QDs were purified and stored in hexane by following the same protocol used for Ros alloy cores.

4. Unknown Alloy (U1). A $CdSe_{0.17}S_{0.83}$ alloy core with an unknown structure was prepared by adding $Cd(BAc)_2$ (0.2 mmol) and ODE (3.6 mL) to a 50 mL r.b.f. and heating to 230 °C. A chalcogen precursor solution (∼0.5 M total chalcogen in ODE) was prepared by mixing TBPSe 0.5 M (0.2 mL), TBPS 1.25 M (0.4 mL), and ODE (0.6 mL). The cores were grown by injecting the chalcogen precursor (0.4 mL) at 230 °C and allowing the reaction to proceed at 220 °C for 50 min. The reaction was quenched by reducing the temperature. The QDs were purified and stored in hexane.

Shell Growth. Three types of shells—composite (*c*) CdS or CdSe, alloy (*a*) $CdSe_{0.5}S_{0.5}$, and gradient alloy (*g*) $CdSe_{0.5}S_{0.5}$ (gradually increasing S or Se content toward the surface)—were grown over the two core materials—CdSe or CdS—to prepare a set of six different (core)shell H-NCs: CdSe-*c*-CdS, CdSe-*a*-CdS, CdSe-*g*-CdS (increasing S toward surface), CdS-*c*-CdSe, CdS-*a*-CdSe, and CdS-*g*-CdSe (increasing Se toward surface). The shells were grown using a standard layer-by-layer process at lower temperatures to minimize anionic diffusion.

Precursors. A Cd precursor solution (0.1 M) was prepared by mixing CdO (1 mmol), OAc (4 mmol), and ODE (8.7 mL) and heating to ∼250 °C under nitrogen until the mixture became a clear and colorless solution. The solution was cooled to ∼100 °C, dried under vacuum for 30 min, flushed with nitrogen, and maintained at ∼50 °C to prevent solidification. A Se precursor solution (0.1 M) was prepared by dissolving Se powder (0.5 mmol) in TBP (5 mL) under nitrogen with sonication until the mixture became a clear, colorless solution. A S precursor solution (0.1 M) was prepared by dissolving $(TMS)_2S$ (0.5 mmol) in TBP (5 mL) under nitrogen.

Layer-by-Layer Shell Growth. In order to prevent homogeneous nucleation of shell materials, the shell was grown in 0.8 monolayer (ML) increment instead of 1 ML. The amounts of shell precursors were calculated based on the volume of each 0.8 ML-thick shell and the total number of cores in the solution, assuming that the shell adopts the lattice parameter of the core. In a typical shell growth reaction, 80−120 nmol of core (CdSe or CdS) was dispersed in a mixture of TD, OLA, and TBP (4:1:1 v/v/v, 4−6 mL) under nitrogen, and the temperature was raised to 190 °C. The Cd precursor for the first 0.8 ML was added dropwise and allowed to react for 15 min. Then, an equimolar amount of chalcogen precursor (S, Se, or mixture of S and Se) was added dropwise and allowed to react for another 15 min, completing the first 0.8 ML shell growth. This cycle was repeated three (3.2 ML) to five (4.8 ML) more times with varying Se-to-S ratios in each cycle to control the internal structures (see Supporting Tables S2 and S3 for the S/Se contents in each layer as well as in the overall nanocrystal). Importantly, the highly efficient reaction was complete in 2−3 h at a relatively low temperature to minimize atomic diffusion. After each 0.8 ML, a 200-μL aliquot was taken and diluted 10-fold in chloroform to monitor the shell growth reaction via absorption and fluorescence spectroscopy. The nanocrystals in each aliquot were purified by precipitating in a mixture of methanol (5 mL) and acetone

DOI: 10.1021/jacs.6b03907
J. Am. Chem. Soc. 2016, 138, 10887−10896

(5 mL) followed by dispersion in hexane for measurement of *QY* and Raman spectra.

Optical and Structural Characterization. Absorption spectra of QD dispersions were obtained using an Agilent Cary 5000 UV−vis−NIR spectrophotometer. Fluorescence spectra were acquired using a Horiba NanoLog spectrofluorometer. Relative fluorescence *QY* values were measured against a reference dye (fluorescein in 1 mM NaOH, *QY* = 0.92).[3] TEM images were acquired using a JEOL 2010 LaB_6 high-resolution microscope in the Frederick Seitz Materials Research Laboratory Central Research Facilities at the University of Illinois. TEM samples were prepared by placing a drop of purified nanocrystal solution in hexane (band edge absorbance ∼0.01) on a TEM grid (Ted Pella #01824), and then wicking away the drop with a tissue. Elemental analysis of CdSeS was performed with a PerkinElmer Optima 2000DV ICP-OES spectrometer in the Microanalysis Laboratory at the University of Illinois. Raman spectra were acquired using a high resolution research grade Horiba LabRAM HR Raman imaging system coupled to an Andor Newton back-illuminated EMCCD DU970P camera (1600 × 200 pixels, thermoelectrically cooled to −70 °C). The excitation wavelength was 532 nm and each Raman spectrum was measured for 10 s with a 100×, NA 0.8 objective, with laser power set to 25 mW using a 1800 g/mm grating with 100 μm slit width. A neutral density filter reduced the incident power to 2.5 mW. The shifts of the Raman spectra were calibrated against a standard Si wafer before measurements. Preliminary scans were performed on samples to ensure that the laser did not alter the sample at different laser powers, for example due to heating,[57] and that the signal was stable over the course of spectrum acquisition. Spectra were background-subtracted in two steps. First, each spectrum was divided by a blank Raman spectrum (acquired under the same conditions) of areas of a Low-E slide on which the sample was deposited to eliminate potential effects of laser fluctuations and contributions from the substrate. Next to remove broad overlapping fluorescence baseline, we subtracted a third degree polynomial function between 140 to 600 cm^{-1} (examples shown in Supporting Figure S7). Spectra depicting representative experimental error are provided in Supporting Figure S8.

EMA Modeling. The electronic energy levels and wave functions of electrons and holes for nanocrystals were calculated using the EMA assuming spherical symmetry and finite energy wells following the original methods of Haus et al.[34] Detailed methods and parameters were described in detail in a recent publication.[58]

MLR Modeling. For Raman spectral analysis, we determined the number of modes contributing to a given band by performing PCA in two spectral ranges for each data set: 140−242 cm^{-1} (CdSe) and 242−350 cm^{-1} (CdS). On the basis of Malinowski's criteria (real error, reduced eigenvalue, and indicator function) the minimal number of sources of variance was found to be 4 and 3 for CdSe and CdS bands, respectively.

We used multiple linear regression (MLR) as a classification method, with class assignment coded as −1 (class 1), 0 (class 2) and 1 (class 3). The integral coding of classes assumes that the class assigned 0 follow a trend intermediate between −1 and 1 classes, which in the case of V_{core} distinguishes the intermediate ternary alloy core values between the binary extremes, and in the case of V_{shell} distinguishes the intermediate gradient shells between the composite and alloy extremes. MLR was performed on parameters obtained from fitting Lorentzian functions to the bands from the full Raman spectra of the nanoparticles. For each of the Lorentzians, four parameters were obtained: position, fwhm, intensity, and area, giving a total of 68 parameters for each spectrum. All of the parameters were mean centered and scaled to unity variance for each of the created models. MLR was used as a variable selection procedure by using a leave one out cross-validation (LOO−CV) as allowed by the relatively small number of samples. Root mean squared error of prediction (RMSEP) was calculated for each of the variables for a given model, assuming a regression using one variable in the first step. In the next step the variable with the lowest RMSEP was added to the model and all other variables were tested in a MLR model with two variables. As shown in Supporting Figure S9, this procedure was repeated for the best 15 parameters, yielding CV curves reaching a minimum RMSEP in the range of 10−14 parameters for predicting core structure, shell structure, and *QY*. For each of the four models the CV curve indicated that 12−13 parameters minimized the prediction error, however, we present models here with lower number of parameters, which still have excellent prediction power, as fewer parameters allow easier interpretation of the physical origin and interaction between parameters, and because LOO−CV has a tendency to create overconstrained models. Thus, we chose the best 7, 9, 8, and 2 parameters to predict the core, the shell with CdSe core, the shell with CdS core, and *QY*, respectively, yielding coefficients tabulated in Figure 3 and Figure 4.

■ ASSOCIATED CONTENT

Supporting Information

The Supporting Information is available free of charge on the ACS Publications website at DOI: 10.1021/jacs.6b03907.

Supporting figures include H-NC electron micrographs, H-NC compositions, additional Raman spectra, spectral trends, and RMSE prediction analysis, and tabulated spectral fitting parameters. (PDF)

■ AUTHOR INFORMATION

Corresponding Authors

*rxb@illinois.edu

*smi@illinois.edu

Notes

The authors declare no competing financial interest.

■ ACKNOWLEDGMENTS

AMS acknowledges support from the NIH (R00CA153914 and R21NS087413). AMS and RB also acknowledge support from the UIUC College of Engineering Strategic Research Initiatives Program and the Mayo-Illinois Alliance. RB acknowledges support from the National Institutes of Health via grant R01EB009745. TPW acknowledges support from Beckman Postdoctoral Fellowship.

■ REFERENCES

(1) Anikeeva, P. O.; Halpert, J. E.; Bawendi, M. G.; Bulovic, V. *Nano Lett.* **2009**, *9*, 2532.

(2) Galland, C.; Ghosh, Y.; Steinbruck, A.; Sykora, M.; Hollingsworth, J. A.; Klimov, V. I.; Htoon, H. *Nature* **2011**, *479*, 203.

(3) Lim, S. J.; Zahid, M. U.; Le, P.; Ma, L.; Entenberg, D.; Harney, A. S.; Condeelis, J. S.; Smith, A. M. *Nat. Commun.* **2015**, *6*, 8210.

(4) Tisdale, W. A.; Williams, K. J.; Timp, B. A.; Norris, D. J.; Aydil, E. S.; Zhu, X. Y. *Science* **2010**, *328*, 1543.

(5) Garcia-Santamaria, F.; Brovelli, S.; Viswanatha, R.; Hollingsworth, J. A.; Htoon, H.; Crooker, S. A.; Klimov, V. I. *Nano Lett.* **2011**, *11*, 687.

(6) Mocatta, D.; Cohen, G.; Schattner, J.; Millo, O.; Rabani, E.; Banin, U. *Science* **2011**, *332*, 77.

(7) Wang, D.; Li, Y. *Adv. Mater.* **2011**, *23*, 1044.

(8) Wang, D. L.; Xin, H. L. L.; Hovden, R.; Wang, H. S.; Yu, Y. C.; Muller, D. A.; DiSalvo, F. J.; Abruna, H. D. *Nat. Mater.* **2013**, *12*, 81.

(9) Chen, C.; Kang, Y. J.; Huo, Z. Y.; Zhu, Z. W.; Huang, W. Y.; Xin, H. L. L.; Snyder, J. D.; Li, D. G.; Herron, J. A.; Mavrikakis, M.; Chi, M. F.; More, K. L.; Li, Y. D.; Markovic, N. M.; Somorjai, G. A.; Yang, P. D.; Stamenkovic, V. R. *Science* **2014**, *343*, 1339.

(10) Robinson, R. D.; Sadtler, B.; Demchenko, D. O.; Erdonmez, C. K.; Wang, L. W.; Alivisatos, A. P. *Science* **2007**, *317*, 355.

(11) Smith, A. M.; Mohs, A. M.; Nie, S. M. *Nat. Nanotechnol.* **2009**, *4*, 56.

(12) Bussian, D. A.; Crooker, S. A.; Yin, M.; Brynda, M.; Efros, A. L.; Klimov, V. I. *Nat. Mater.* **2009**, *8*, 35.

DOI: 10.1021/jacs.6b03907
J. Am. Chem. Soc. 2016, 138, 10887−10896

(13) Zhang, J. T.; Tang, Y.; Lee, K.; Min, O. Y. *Science* **2010**, *327*, 1634.
(14) Shi, W. L.; Zeng, H.; Sahoo, Y.; Ohulchanskyy, T. Y.; Ding, Y.; Wang, Z. L.; Swihart, M.; Prasad, P. N. *Nano Lett.* **2006**, *6*, 875.
(15) Jin, Y. D.; Jia, C. X.; Huang, S. W.; O'Donnell, M.; Gao, X. H. *Nat. Commun.* **2010**, *1*, 41.
(16) Chaudhuri, R. G.; Paria, S. *Chem. Rev.* **2012**, *112*, 2373.
(17) Mashford, B. S.; Stevenson, M.; Popovic, Z.; Hamilton, C.; Zhou, Z. Q.; Breen, C.; Steckel, J.; Bulovic, V.; Bawendi, M.; Coe-Sullivan, S.; Kazlas, P. T. *Nat. Photonics* **2013**, *7*, 407.
(18) Nozik, A. J.; Beard, M. C.; Luther, J. M.; Law, M.; Ellingson, R. J.; Johnson, J. C. *Chem. Rev.* **2010**, *110*, 6873.
(19) Ip, A. H.; Thon, S. M.; Hoogland, S.; Voznyy, O.; Zhitomirsky, D.; Debnath, R.; Levina, L.; Rollny, L. R.; Carey, G. H.; Fischer, A.; Kemp, K. W.; Kramer, I. J.; Ning, Z.; Labelle, A. J.; Chou, K. W.; Amassian, A.; Sargent, E. H. *Nat. Nanotechnol.* **2012**, *7*, 577.
(20) Choi, H. S.; Liu, W.; Liu, F.; Nasr, K.; Misra, P.; Bawendi, M.; Frangioni, J. V. *Nat. Nanotechnol.* **2010**, *5*, 42.
(21) Kairdolf, B. A.; Smith, A. M.; Stokes, T. H.; Wang, M. D.; Young, A. N.; Nie, S. M. *Annu. Rev. Anal. Chem.* **2013**, *6*, 143.
(22) Zrazhevskiy, P.; Gao, X. H. *Nat. Commun.* **2013**, *4*, 1619.
(23) Xie, R. G.; Kolb, U.; Li, J. X.; Basche, T.; Mews, A. *J. Am. Chem. Soc.* **2005**, *127*, 7480.
(24) Bae, W. K.; Padilha, L. A.; Park, Y. S.; McDaniel, H.; Robel, I.; Pietryga, J. M.; Klimov, V. I. *ACS Nano* **2013**, *7*, 3411.
(25) Bailey, R. E.; Nie, S. M. *J. Am. Chem. Soc.* **2003**, *125*, 7100.
(26) Baranov, A. V.; Rakovich, Y. P.; Donegan, J. F.; Perova, T. S.; Moore, R. A.; Talapin, D. V.; Rogach, A. L.; Masumoto, Y.; Nabiev, I. *Phys. Rev. B: Condens. Matter Mater. Phys.* **2003**, *68*, 165306.
(27) Dzhagan, V. M.; Valakh, M. Y.; Milekhin, A. G.; Yeryukov, N. A.; Zahn, D. R. T.; Cassette, E.; Pons, T.; Dubertret, B. *J. Phys. Chem. C* **2013**, *117*, 18225.
(28) Todescato, F.; Minotto, A.; Signorini, R.; Jasieniak, J. J.; Bozio, R. *ACS Nano* **2013**, *7*, 6649.
(29) Han, P.; Bester, G. *Phys. Rev. B: Condens. Matter Mater. Phys.* **2015**, *92*, 125438.
(30) Gouadec, G.; Colomban, P. *J. Raman Spectrosc.* **2007**, *38*, 598.
(31) Qiu, X.; Chen, L.; Gong, H.; Zhu, M.; Han, J.; Zi, M.; Yang, X.; Ji, C.; Cao, B. *J. Colloid Interface Sci.* **2014**, *430*, 200.
(32) Moon, G. D.; Ko, S.; Min, Y.; Zeng, J.; Xia, Y.; Jeong, U. *Nano Today* **2011**, *6*, 186.
(33) Shaw, D. *J. Cryst. Growth* **1988**, *86*, 778.
(34) Haus, J. W.; Zhou, H. S.; Honma, I.; Komiyama, H. *Phys. Rev. B: Condens. Matter Mater. Phys.* **1993**, *47*, 1359.
(35) Dabbousi, B. O.; Rodriguez-Viejo, J.; Mikulec, F. V.; Heine, J. R.; Mattoussi, H.; Ober, R.; Jensen, K. F.; Bawendi, M. G. *J. Phys. Chem. B* **1997**, *101*, 9463.
(36) Kim, S.; Fisher, B.; Eisler, H. J.; Bawendi, M. *J. Am. Chem. Soc.* **2003**, *125*, 11466.
(37) Smith, A. M.; Nie, S. M. *Acc. Chem. Res.* **2010**, *43*, 190.
(38) Swafford, L. A.; Weigand, L. A.; Bowers, M. J.; McBride, J. R.; Rapaport, J. L.; Watt, T. L.; Dixit, S. K.; Feldman, L. C.; Rosenthal, S. J. *J. Am. Chem. Soc.* **2006**, *128*, 12299.
(39) Mlayah, A.; Brugman, A. M.; Carles, R.; Renucci, J. B.; Valakh, M. Y.; Pogorelov, A. V. *Solid State Commun.* **1994**, *90*, 567.
(40) Beserman, R. *Solid State Commun.* **1977**, *23*, 323.
(41) Gomonnai, A. V.; Azhniuk, Y. M.; Yukhymchuk, V. O.; Kranjčec, M.; Lopushansky, V. V. *Phys. Status Solidi B* **2003**, *239*, 490.
(42) Adachi, S. In *Properties of Semiconductor Alloys: Group-IV, III-V and II-VI Semiconductors*; Wiley, 2009.
(43) Azhniuk, Y. M.; Milekhin, A. G.; Gomonnai, A. V.; Lopushansky, V. V.; Yukhymchuk, V. O.; Schulze, S.; Zenkevich, E. I.; Zahn, D. R. T. *J. Phys.: Condens. Matter* **2004**, *16*, 9069.
(44) Klein, M. C.; Hache, F.; Ricard, D.; Flytzanis, C. *Phys. Rev. B: Condens. Matter Mater. Phys.* **1990**, *42*, 11123.
(45) Lin, C.; Gong, K.; Kelley, D. F.; Kelley, A. M. *ACS Nano* **2015**, *9*, 8131.
(46) Malinowski, E. R. *Factor Analysis in Chemistry*, 3rd ed.; Wiley, 2002.
(47) Brereton, R. G. *Chemometrics: Data Analysis for the Laboratory and Chemical Plant*; Wiley, 2003.
(48) Dzhagan, V. M.; Lokteva, I.; Valakh, M. Y.; Raevska, O. E.; Kolny-Olesiak, J.; Zahn, D. R. T. *J. Appl. Phys.* **2009**, *106*, 084318.
(49) Adachi, S. *Properties of Group-IV, III-V and II-VI Semiconductors*; Wiley, 2005.
(50) Meulenberg, R. W.; Jennings, T.; Strouse, G. F. *Phys. Rev. B: Condens. Matter Mater. Phys.* **2004**, *70*, 235311.
(51) Tschirner, N.; Lange, H.; Schliwa, A.; Biermann, A.; Thomsen, C.; Lambert, K.; Gomes, R.; Hens, Z. *Chem. Mater.* **2012**, *24*, 311.
(52) Kelley, A. M.; Dai, Q.; Jiang, Z.-j.; Baker, J. A.; Kelley, D. F. *Chem. Phys.* **2013**, *422*, 272.
(53) Dzhagan, V. M.; Valakh, M. Y.; Raevskaya, A. E.; Stroyuk, A. L.; Kuchmiy, S. Y.; Zahn, D. R. T. *Nanotechnology* **2007**, *18*, 285701.
(54) Dzhagan, V.; Lokteva, I.; Himcinschi, C.; Jin, X.; Kolny-Olesiak, J.; Zahn, D. R. *Nanoscale Res. Lett.* **2011**, *6*, 1.
(55) Lim, S. J.; Ma, L.; Schleife, A.; Smith, A. M. *Coord. Chem. Rev.* **2016**, *320-321*, 216.
(56) Aubert, T.; Cirillo, M.; Flamee, S.; Van Deun, R.; Lange, H.; Thomsen, C.; Hens, Z. *Chem. Mater.* **2013**, *25*, 2388.
(57) Faraci, G.; Gibilisco, S.; Pennisi, A. R. *Phys. Rev. B: Condens. Matter Mater. Phys.* **2009**, *80*, 193410.
(58) Smith, A. M.; Lane, L. A.; Nie, S. M. *Nat. Commun.* **2014**, *5*, 4506.

DOI: 10.1021/jacs.6b03907
J. Am. Chem. Soc. 2016, 138, 10887−10896